JM PAPERS

Scaling regimes in rapidly rotating thermal convection at extreme Rayleigh numbers

Jiaxing Song[1],†, **Olga Shishkina**[2],† and **Xiaojue Zhu**[1],†

[1]Max Planck Institute for Solar System Research, 37077 Göttingen, Germany

[2]Max Planck Institute for Dynamics and Self-Organization, 37077 Göttingen, Germany

The geostrophic turbulence in rapidly rotating thermal convection exhibits characteristics shared by many highly turbulent geophysical and astrophysical flows. In this regime, the convective length and velocity scales and heat flux are all diffusion-free, i.e. independent of the viscosity and thermal diffusivity. Our direct numerical simulations (DNS) of rotating Rayleigh–Bénard convection in domains with no-slip top and bottom and periodic lateral boundary conditions for a fluid with the Prandtl number $Pr = 1$ and extreme buoyancy and rotation parameters (the Rayleigh number up to $Ra = 3 \times 10^{13}$ and the Ekman number down to $Ek = 5 \times 10^{-9}$) indeed demonstrate all these diffusion-free scaling relations, in particular, that the dimensionless convective heat transport scales with the supercriticality parameter $\widetilde{Ra} \equiv Ra \, Ek^{4/3}$ as $Nu - 1 \propto \widetilde{Ra}^{3/2}$, where Nu is the Nusselt number. We further derive and verify in the DNS that with the decreasing $\widetilde{Ra}$, the geostrophic turbulence regime undergoes a transition into another geostrophic regime, the convective heat transport in this regime is characterized by a very steep $\widetilde{Ra}$-dependence, $Nu - 1 \propto \widetilde{Ra}^3$.

Key words: Bénard convection, geostrophic turbulence, turbulent convection

1. Introduction

Turbulent rotating convection (Ecke & Shishkina 2023) is a fundamental mechanism that drives the heat and momentum transport in planets (Busse & Carrigan 1976; Ahlers, Grossmann & Lohse 2009; Wicht & Sanchez 2019), as well as being the energy source for planetary and stellar magnetic fields (Jones 2011; Aurnou *et al.* 2015; Guervilly, Cardin &

† Email addresses for correspondence: song@mps.mpg.de, olga.shishkina@ds.mpg.de, zhux@mps.mpg.de

Schaeffer 2019). The parameters of the astrophysical and geophysical flows are too extreme to be realized nowadays in lab experiments and direct numerical simulations (DNS). For example, in the Earth's core, the Ekman number $Ek \equiv \nu/(2\Omega L^2)$, which is the inverse of the dimensionless rotating rate, can be as low as 10^{-15}, and the Reynolds number $Re \equiv uL/\nu$, which is the dimensionless flow velocity, can be as high as 10^9 (Aurnou *et al.* 2015; Plumley & Julien 2019). Here, ν is the kinematic viscosity, Ω is the rotating angular velocity, u is the characteristic velocity, and L is the domain length scale. To estimate the heat and momentum transport in a particular geophysical or astrophysical system, one needs first, the scaling relations that hold in the corresponding flow regime, and second, measurements or simulations for a certain range of control parameters, which are not as extreme as in the considered geophysical or astrophysical system, but which anyway belong to the same scaling regime as the considered system. As soon as both objectives are achieved, the results from the labs and supercomputers can be upscaled to the geophysical and astrophysical conditions.

Rotating Rayleigh–Bénard convection (RRBC) (Kunnen 2021; Ecke & Shishkina 2023) is the most studied set-up of rotating thermal convection. Here, a container of height L and temperature difference Δ between its bottom and top is rotated with angular velocity Ω about its centrally located vertical axis. The main control parameters of the system are Ek, the Rayleigh number $Ra \equiv \alpha_T g L^3 \Delta/(\kappa\nu)$, which is the dimensionless temperature difference across the domain, and the Prandtl number $Pr \equiv \nu/\kappa$, a material property. Here, α_T is the thermal expansion coefficient, g is the gravitational acceleration, and κ is the thermal diffusivity. The main dimensionless response characteristics are Re and the Nusselt number Nu, which is the total vertical heat flux normalized by the purely conductive counterpart.

The scaling relations for the heat (Nu) and momentum (Re) transfer are usually sought as functions of Ek, Ra and Pr, expressed in forms $\sim Ra^\alpha Ek^\beta Pr^\gamma$. For RRBC, under the assumption that the heat flux is independent of ν and κ, a diffusion-free heat transfer scaling law $Nu \sim Ra^{3/2} Ek^2 Pr^{-1/2}$ can be derived (Stevenson 1979; Gillet & Jones 2006; Julien *et al.* 2012*a*,*b*; Gastine, Wicht & Aubert 2016; Plumley *et al.* 2017; Plumley & Julien 2019; Aurnou, Horn & Julien 2020; Bouillaut *et al.* 2021). This relation is associated with the geostrophic turbulence regime, where not only the heat flux but also the whole system is independent of ν and κ (Schmitz & Tilgner 2009; Julien *et al.* 2012*a*; Plumley *et al.* 2017; Guervilly *et al.* 2019; Bouillaut *et al.* 2021; Wang *et al.* 2021), following the Kolmogorov energy cascade picture (Ahlers *et al.* 2009). Worldwide efforts over the past decade have been devoted to achieving and verifying this diffusion-free Nu scaling by designing increasingly taller rotating convection cells (Cheng *et al.* 2018; Ecke & Shishkina 2023). This regime was also studied in a recent experiment where convection is driven radiatively, with reduced models, and in DNS with free-slip boundary conditions (BCs) (Julien *et al.* 2012*a*; Stellmach *et al.* 2014; Plumley *et al.* 2017; Bouillaut *et al.* 2021). There, to make the resolution and rotation rate manageable, the typical Ek value is of the order of 10^{-7} at least, and Ra is of the order of 10^{12} at most. However, it is yet to be seen whether this scaling can be achieved in experiments and DNS with the traditional lab settings (no-slip BCs, the only option for most of the experiments).

In the limit of rapid rotation ($Ek \to 0$), strong thermal forcing ($Ra \to \infty$) and infinite Pr, from the asymptotically reduced equations for $Ra\, Ek^{8/5} = O(1)$, an upper bound $Nu \leq 20.56(Ra/Ra_c)^3 \propto \widetilde{Ra}^3$ was derived in Grooms & Whitehead (2015), where Ra_c is the critical Ra for the onset of RRBC, and $\widetilde{Ra} \equiv Ra\, Ek^{4/3}$. Here, Nu increases much faster than in the regime of geostrophic turbulence. One comes to a similar scaling relation, for
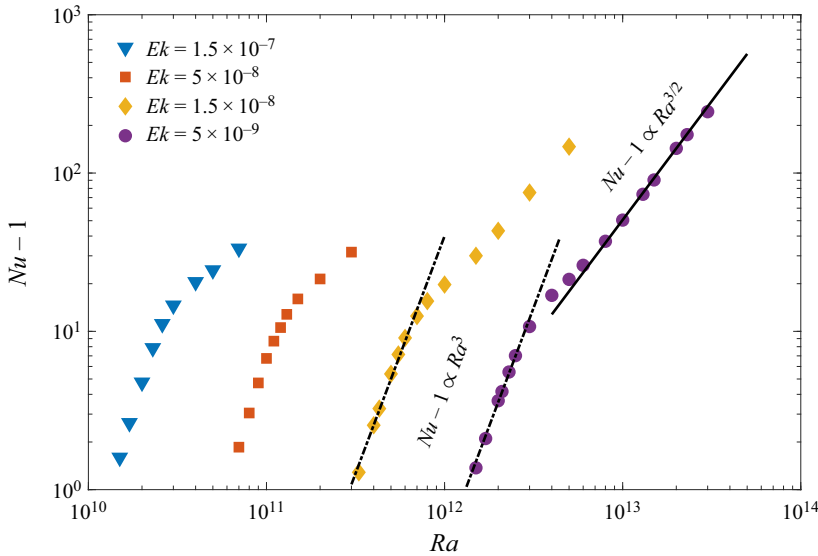
Figure 1. Convective heat transport $Nu - 1$ as a function Ra, for different Ek values and $Pr = 1$. All studied cases correspond to the rotation-dominated regime of RRBC (the Rossby number is $Ro \ll 1$). One can see that when Ra is sufficiently large and Ek sufficiently small, $Nu - 1$ scales as $\propto Ra^3$ for relatively smaller values of Ra, and as $\propto Ra^{3/2}$ for larger Ra.

any Pr, under the assumption that the total vertical heat flux is independent of the fluid layer depth L (but not of κ and ν as in the geostrophic turbulence regime). This assumption immediately gives the scaling relations $Nu \propto Ra^{1/3}$ for the case of weak or no rotation (Malkus 1954; Priestley 1959), and $Nu \propto \widetilde{Ra}^3$ for the case of rotation dominance, see e.g. Boubnov & Golitsyn (1990) and King, Stellmach & Aurnou (2012). Although such scaling of Nu with the control parameters was observed in some experiments and simulations for no-slip BCs at the plates and periodic lateral BCs (King *et al.* 2012; Stellmach *et al.* 2014; Cheng *et al.* 2015; Cheng & Aurnou 2016; Julien *et al.* 2016; Aguirre Guzmán *et al.* 2021; Lu *et al.* 2021), the behaviour of Re and convective length scales in that regime remains unclear. Also unclear is how this regime is connected to the regime of geostrophic turbulence.

In this work, we present results of the DNS of RRBC for $Pr = 1$ and extreme parameter range for Ra from 1.5×10^{10} to 3×10^{13}, and Ek from 1.5×10^{-7} down to 5×10^{-9} (see figure 1 for the parameter space). For the first time, we derive both geostrophic regimes within a new unifying theoretical framework, achieve both regimes in our DNS, and show the scaling relations for Nu and Re, the convective length scale, kinetic energy and thermal dissipation rates in both regimes. The proposed scaling argument can be used as a simple framework for deriving not only the heat transfer, but also the flow speed as well as convective length scale scaling relations in different flow regimes in rotating convection. The transition between the two regimes is seen in the scalings of all quantities; however, the scaling with Ra and Ek of the convective bulk length scale ℓ remains the same in both regimes. Note that this transition between the two rotation-dominated regimes is of course very different from the transition between the rotation dominance and the gravitational buoyancy dominance in RRBC (Stevens, Clercx & Lohse 2013; Kunnen 2021; Ecke & Shishkina 2023). For a discussion of the latter transition, we refer to (Ecke & Shishkina 2023, § 3.3).

2. Numerical details

The Boussinesq approximation is used to describe RRBC of a fluid between two horizontal plates, which is rotated with a constant angular velocity Ω around the vertical axis z, under gravitational acceleration $g = -ge_z$, where e_z is the vertical unit vector. The chosen reference scales are the height of the domain L, the temperature difference between the plates Δ, and the characteristic free-fall velocity $U_{ff} = \sqrt{g\alpha_T L\Delta}$. Non-dimensional temperature θ, velocity u, pressure p and time t are obtained using these scales. The dimensionless governing equations for the incompressible fluid are $\nabla \cdot u = 0$,

$$\frac{\partial u}{\partial t} + u \cdot \nabla u = -\nabla p + \sqrt{\frac{Pr}{Ra}}\nabla^2 u + \theta e_z - \frac{1}{Ek}\sqrt{\frac{Pr}{Ra}}\,e_z \times u, \qquad (2.1)$$

$$\frac{\partial \theta}{\partial t} + u \cdot \nabla \theta = \frac{1}{\sqrt{Ra\,Pr}}\nabla^2 \theta. \qquad (2.2)$$

No-slip boundaries and constant temperature conditions at the bottom and top plates were applied. We consider periodic BCs in horizontal directions, to avoid the wall modes in rapidly RRBC (Ecke, Zhong & Knobloch 1992; Herrmann & Busse 1993; Favier & Knobloch 2020; Shishkina 2020; de Wit *et al.* 2020, 2023; Zhang *et al.* 2020; Zhang, Ecke & Shishkina 2021; Ecke, Zhang & Shishkina 2022). To solve the governing equations, an energy-conserving second-order finite-difference code AFiD was utilized (Verzicco & Orlandi 1996; van der Poel *et al.* 2015; Zhu *et al.* 2018). The original code was updated to include a Coriolis force term in the momentum equations to account for system rotation. The code was parallelized using a two-dimensional pencil domain decomposition strategy, allowing it to effectively handle large-scale computations (van der Poel *et al.* 2015). In every studied case, the computational domain size is large enough to capture the typical flow structures: specifically, the horizontal extension of the domain is at least 20 times larger than the onset convective length scale $2.4\,Ek^{1/3}$. The computational grids are fine enough to the resolve Kolmogorov microscales in the bulk and in the boundary layers (Shishkina *et al.* 2010). Thus the maximal value of the ratio of the mesh size to the mean Kolmogorov microscale is always smaller than 2.2, even for the highest $Ra = 3.0 \times 10^{13}$. There are always at least 10 grid points in each thermal and viscous (Ekman) boundary layer. For example, at $Ra = 3.0 \times 10^{13}$, $Ek = 5.0 \times 10^{-9}$ with aspect ratio 0.125, $N_z \times N_x \times N_y = 2048 \times 1024 \times 1024$ grid points are used in the vertical (N_z) and two horizontal (N_x, N_y) directions. Additionally, simulations lasting at least 400 free-fall time units were performed to ensure that statistically steady flow states are achieved. The convergence of the Nusselt numbers is checked for the entire domain. In this study, the maximum relative errors of the Nusselt numbers calculated by five different methods listed in Appendix A were less than 1 % (see table 3).

3. Results

In what follows, we assume that in any rotation-dominated regime, the dimensionless convective heat transport is proportional to a power function of the supercriticality parameter $\widetilde{Ra} \equiv Ra\,Ek^{4/3}$ (see e.g. Julien *et al.* 2012a; Stellmach *et al.* 2014),

$$Nu - 1 \propto \widetilde{Ra}^{\xi}, \qquad (3.1)$$

with different exponents ξ in different regimes. First, we discuss relations that hold in both studied rotation-dominated regimes and recall the rigorous relations for the

time- and volume-averaged kinetic energy dissipation rate $\epsilon_u = \langle \nu(\partial_i u_j(\boldsymbol{x}, t))^2 \rangle$ and thermal dissipation rate $\epsilon_\theta = \langle \kappa(\partial_i \theta(\boldsymbol{x}, t))^2 \rangle$ that hold in RRBC (Ahlers *et al.* 2009):

$$\epsilon_u = (\nu^3/L^4)(Nu - 1) \, Ra \, Pr^{-2}, \tag{3.2}$$

$$\epsilon_\theta = \kappa(\Delta^2/L^2) \, Nu. \tag{3.3}$$

We introduce u, θ and ℓ, which are the representative convective scales for, respectively, the velocity, temperature and length. The total heat flux can be decomposed into a conductive contribution $\kappa \Delta/L$ and a convective contribution q that scales as $q \sim u\theta$. The dimensionless convective heat flux then scales as

$$Nu - 1 \sim \frac{q}{\kappa \Delta/L} \sim \frac{u\theta}{\kappa \Delta/L}. \tag{3.4}$$

Analogously, the total thermal dissipation rate ϵ_θ can be decomposed into a conductive contribution $\kappa \Delta^2/L^2$ and a convective contribution $\tilde{\epsilon}_\theta$, which scales as $\tilde{\epsilon}_\theta \sim u\theta^2/\ell$. This, in combination with (3.3), gives

$$Nu - 1 \sim \frac{\tilde{\epsilon}_\theta}{\kappa \Delta^2/L^2} \sim \frac{\theta^2}{\Delta^2} \frac{L}{\ell} \frac{uL}{\nu} \frac{\nu}{\kappa}. \tag{3.5}$$

Combining (3.4) and (3.5), we obtain $\ell/L \sim \theta/\Delta$, which together with (3.5) leads to

$$Nu - 1 \sim \frac{\theta^2}{\Delta^2} \frac{L}{\ell} Re \, Pr \sim \frac{\ell}{L} Re \, Pr. \tag{3.6}$$

The same scaling relation (3.6) has also been applied to quasi-static magnetoconvection (Bader & Zhu 2023). In a turbulent flow, ϵ_u scales as $\epsilon_u \sim u^3/\ell$, which can also be obtained from the Coriolis, inertia and Archimedean force balance (Landau & Lifshitz 1987; Gastine *et al.* 2016; Madonia *et al.* 2023). This, in combination with (3.2) and (3.6), leads to

$$Re \sim (\ell/L) \, Pr^{-1/2} \, Ra^{1/2}, \tag{3.7}$$

$$Nu - 1 \sim (\ell/L)^2 \, Pr^{1/2} \, Ra^{1/2}. \tag{3.8}$$

The dimensional convective bulk length scale ℓ is diffusion-free in the geostrophic turbulence regime, meaning that it is independent of ν and κ. If ℓ/L is thought of as a product of power functions of Ra, Ek and Pr, then the requirement for ℓ/L to be diffusion-free, i.e. $\ell/L \propto \nu^0 \kappa^0$, means that ℓ/L must scale as

$$\ell/L \sim Ra^a \, Ek^{2a} \, Pr^{-a} \tag{3.9}$$

for some value of a. From (3.8) and (3.9), it follows that

$$Nu - 1 \propto \widetilde{Ra}^{2a+1/2} \, Ek^{(4a-2)/3}. \tag{3.10}$$

From (3.1) and (3.10), we derive $a = 1/2$ and $\xi = 3/2$, therefore the following relations must be fulfilled:

$$\ell/L \sim Ra^{1/2} \, Ek \, Pr^{-1/2}, \tag{3.11}$$

$$Nu - 1 \sim Ra^{3/2} \, Ek^2 \, Pr^{-1/2}, \tag{3.12}$$

$$Re \sim Ra \, Ek \, Pr^{-1}, \tag{3.13}$$

$$(L^4/\nu^3)\epsilon_u \sim Ra^{5/2} \, Ek^2 \, Pr^{-5/2}. \tag{3.14}$$

Note that $a = 1/2$ means that ℓ/L scales as the Rossby number $Ro \equiv \sqrt{Ra/Pr}\, Ek$. Equations (3.11)–(3.14) show that in the geostrophic turbulence regime, the dimensional convective bulk length scale ℓ and velocity scale $\nu Re/L$, the convective heat flux $\kappa\Delta/L(Nu-1)$ and the dissipation rates are all diffusion-free; they all scale as $\propto \nu^0\kappa^0$. Some of the scaling relations (3.11)–(3.13) for the geostrophic turbulence were proposed in Aurnou *et al.* (2020); see also Sprague *et al.* (2006), Julien *et al.* (2012*b*), Plumley & Julien (2019), Guervilly *et al.* (2019) and Ecke & Shishkina (2023). Previously, the scaling relations for Nu, Re and ℓ without diffusion effects were proposed independently through various theories and analyses. Our scaling argument unifies the picture and suggests that all three scaling relations (3.11)–(3.13) should hold simultaneously to characterize the system as a geostrophic turbulence regime.

One can argue that ℓ can be non-dimensionalized (without involving ν or κ) not only with L but in another way, using e.g. $\alpha_T\Delta g/\Omega^2$ as the reference length. In that case the diffusion-free length scale would imply $\ell/(\alpha_T\Delta g/\Omega^2) \sim Ra^b\, Ek^{2b}\, Pr^{-b}$ for some b, which is equivalent to $\ell/L \sim Ra^{1+b}\, Ek^{2b+2}\, Pr^{-1-b}$. Combining this with (3.8) and (3.1), we derive that $b = -1/2$ and $\xi = 3/2$, and that the scaling relations for the geostrophic turbulence, that is, (3.11)–(3.14), should hold anyway.

To verify the scaling relations (3.11)–(3.14), we have conducted DNS of RRBC in domains with periodic lateral BCs, in order to avoid the effect of the wall modes (Rossby 1969; Favier & Knobloch 2020) or boundary zonal flows (Zhang *et al.* 2020; Wedi *et al.* 2022). The studied cases in the DNS parameter range are unprecedented: Ra up to 3×10^{13}, and Ek down to 5×10^{-9}. First, we verify that ℓ/L scales according to (3.11). It is indeed fulfilled, since $(\ell/L)\, Ra\, Ek$ scales as

$$(\ell/L)\, Ra\, Ek \propto Ra^{3/2}\, Ek^2 = \widetilde{Ra}^{3/2}. \tag{3.15}$$

This is supported by the DNS data presented in figure 2(*a*). Here, following Guervilly, Hughes & Jones (2014), Guervilly *et al.* (2019) and Maffei *et al.* (2021), we conduct the two-dimensional (2-D) Fourier transforms of the instantaneous vertical velocity u_z at the mid-height, in order to evaluate ℓ/L as $\ell/L = \sum_{k_h}[\hat{u}_z(k_h)\,\hat{u}_z^*(k_h)] / \sum_{k_h} k_h[\hat{u}_z(k_h)\,\hat{u}_z^*(k_h)]$, where $\hat{u}_z(k_h)$ and $\hat{u}_z^*(k_h)$ are, respectively, the 2-D Fourier transforms of u_z and its complex conjugate, and $k_h \equiv (k_x^2 + k_y^2)^{1/2}$ is the horizontal wavenumber. The use of other quantities to evaluate the convective length scale leads to similar results. Here, we also conduct the 2-D Fourier transforms of the temperature fluctuations $\theta' = \theta - \langle\theta\rangle$ to calculate the convective length scale ℓ_θ/L. As demonstrated in figure 3, the convective length scale follows the scaling of $Ra^{1/2}\, Ek$ in two regimes: one is the low $Ra\, Ek^{4/3} \leq 30$ regime, and the other is the high $Ra\, Ek^{4/3} \geq 80$ regime.

As assumed in (3.1), $Nu - 1$ indeed behaves as a function of $\widetilde{Ra}$, since all data from figure 1 follow a master curve when plotted versus $\widetilde{Ra}$; see figure 2(*b*). For large values of $\widetilde{Ra}$, $Nu - 1$ scales according to (3.12), as expected. At $\widetilde{Ra} \approx 30$, one observes a transition to some other regime for lower $\widetilde{Ra}$, with a steeper growth of Nu.

To verify the theoretical predictions on the Re-scaling in the geostrophic turbulence regime, we notice that $Re\, Ek^{1/3}$ should scale as $\propto \widetilde{Ra}$ if relation (3.13) holds. Indeed, the data in figure 2(*c*) support this scaling relation for large $\widetilde{Ra}$. Here, following Guervilly *et al.* (2014, 2019), Gastine *et al.* (2016) and Maffei *et al.* (2021), in order to minimize the impact from the large-scale vortices and properly characterize the amplitude of convective bulk motions and evaluate Re, we use the vertical velocity u_z as the typical velocity scale: $Re = \sqrt{\langle u_z^2\rangle}\, L/\nu$. Note that our DNS as well as previous DNS for periodic lateral BCs
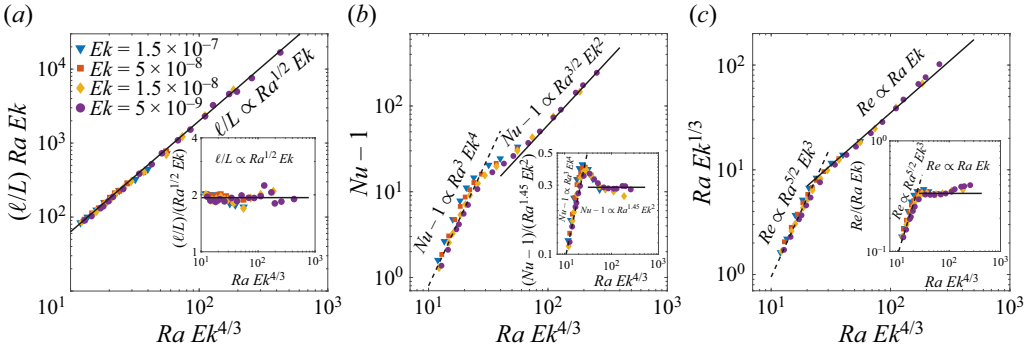
Figure 2. Dimensionless (*a*) convective length scale ℓ/L (multiplied by $Ra\,Ek$), (*b*) heat transport $Nu - 1$, and (*c*) Re (multiplied by $Ek^{1/3}$), as functions of $\widetilde{Ra}$, for all DNS data from figure 1. The DNS demonstrate $\ell/L \sim Ro$. (*a*) The inset shows ℓ/L, normalized by Ro. (*b*) The data for different Ek fall on one graph. For larger $\widetilde{Ra}$, $Nu - 1$ scales as expected for the geostrophic turbulence regime, i.e. $Nu - 1 \propto \widetilde{Ra}^{3/2}$ (solid line), while for smaller $\widetilde{Ra}$, one observes a transition to a regime with $Nu - 1 \propto \widetilde{Ra}^3$ (dashed line). In the inset, the same data are presented in a compensated way, where the normalization is chosen according to the best fit of the data for $Ek = 5 \times 10^{-9}$ and large values of Ra, $Nu - 1 \propto Ra^{1.45 \pm 0.05}$. (*c*) For larger $\widetilde{Ra}$, Re scales almost as expected for the geostrophic turbulence regime: $Re \propto Ra\,Ek$ (solid line), while for smaller $\widetilde{Ra}$, it scales as $Re \propto Ra^{5/2}\,Ek^3$ (dashed line). In the inset, Re, normalized by its scaling in the geostrophic diffusion-free regime, i.e. $Re/(Ra\,Ek)$, is plotted versus $\widetilde{Ra}$.
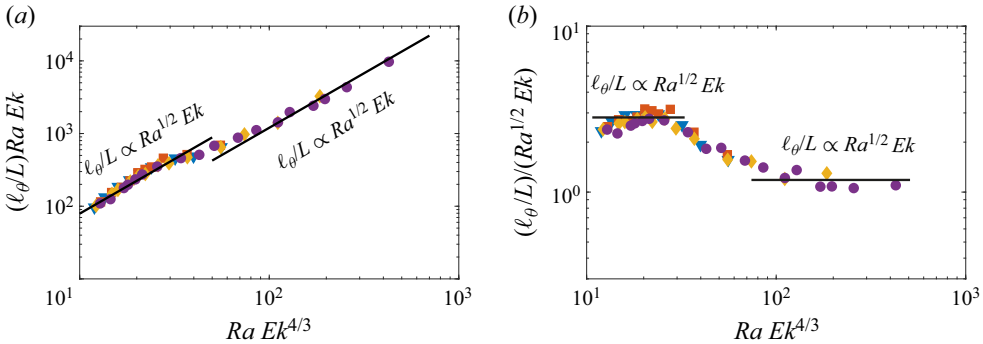

Figure 3. (*a*) Dimensionless convective length scale ℓ_θ/L (multiplied by $Ra\,Ek$) evaluated by the temperature fluctuations, and (*b*) its compensation with $Ra^{1/2}\,Ek$ as a function of $Ra\,Ek^{4/3}$. Symbols have the same meanings as in figure 1.

show formation of large-scale vortices in the geostrophic turbulence regime, which is also associated with an additional increase of Re for larger $\widetilde{Ra}$ (Julien *et al.* 2012*a*,*b*; de Wit *et al.* 2022). Thus all shown scalings of ℓ/L, $Nu - 1$ and Re for large $\widetilde{Ra}$ follow the predictions (3.11)–(3.13) for the geostrophic turbulence regime.

In order to quantify the quality of the agreement between the derived diffusion-free scaling relations and the DNS data, we fit the exponents of the heat transport scaling $Nu - 1 \propto Ra^\alpha\,Ek^2$, the velocity scaling $Re \propto Ra^\beta\,Ek$, and the convective length scale scaling $\ell/L \propto Ra^\gamma\,Ek$, based on different Ra ranges of data points for $Ek = 5 \times 10^{-9}$. The results are listed in table 1. As demonstrated in table 1, with 95 % confidence, the heat transport scaling exponent α ranges from 1.42 to 1.48, the momentum transport scaling exponent β ranges from 1.16 to 1.18, and the convective length scale scaling exponent γ ranges from 0.46 to 0.70, with variant fitting data points. The values of the exponents α and β do not change much with the changing number of the fitting data points, while the

Theory	—	$\alpha = 1.5$	$\beta = 1.0$	$\gamma = 0.5$
Points	*Ra* range	α range	β range	γ range
4	8.0×10^{12}–1.5×10^{13}	1.42 ± 0.05	1.17 ± 0.14	0.70 ± 0.5
5	8.0×10^{12}–2.0×10^{13}	1.47 ± 0.09	1.18 ± 0.07	0.62 ± 0.26
6	8.0×10^{12}–2.3×10^{13}	1.48 ± 0.06	1.18 ± 0.06	0.50 ± 0.25
7	8.0×10^{12}–3.0×10^{13}	1.45 ± 0.05	1.16 ± 0.04	0.46 ± 0.18

Table 1. The theoretical and least squares fit exponents of $Nu - 1 \propto Ra^{\alpha} Ek^2$, $Re \propto Ra^{\beta} Ek$ and $\ell/L \propto Ra^{\gamma} Ek$ of the geostrophic turbulence regime. The least squares fit is conducted at the smallest $Ek = 5 \times 10^{-9}$, with different data points, with 95 % confidence. The first data point is chosen at $Ra = 8.0 \times 10^{12}$, where the geostrophic turbulence regime begins to set in.

value of the exponent γ is quite sensitive to the fitting *Ra* range, and it seems to converge to the predicted theoretical value when fitting with more data points.

But what is the regime of a steeper growth of $Nu - 1$ and *Re* that we observe for smaller $\widetilde{Ra}$ ($\widetilde{Ra} \lesssim 30$) in figure 2? How can we understand its scaling relations theoretically?

For any given *Ek*, with decreasing $\widetilde{Ra}$, the flow should gradually laminarize, and the ϵ_u-scaling should undergo transition to the scaling $\epsilon_u \sim \nu u^2/\ell^2$. This relation, in combination with (3.2) and (3.6), leads to

$$Re \sim (\ell/L)^3 Pr^{-1} Ra, \tag{3.16}$$

$$Nu - 1 \sim (\ell/L)^4 Ra. \tag{3.17}$$

The DNS data show that in this regime of lower $\widetilde{Ra}$, the convective bulk length scale ℓ/L is also proportional to $Ra^{1/2} Ek$; see figure 2(*a*). From this, (3.17) and (3.1), we obtain $\xi = 3$, meaning a steeper growth of *Re* and *Nu* with increasing $\widetilde{Ra}$:

$$\ell/L \propto Ra^{1/2} Ek, \tag{3.18}$$

$$Nu - 1 \propto Ra^3 Ek^4, \tag{3.19}$$

$$Re \propto Ra^{5/2} Ek^3, \tag{3.20}$$

$$(L^4/\nu^3)\epsilon_u \propto Ra^4 Ek^4. \tag{3.21}$$

The steep *Nu*-scaling (3.19) was derived in Boubnov & Golitsyn (1990), where the marginal thermal boundary layer instability in rotating convection was considered. The steep heat transfer scaling $Nu - 1 \sim Ra^3 Ek^4$ can be considered as an asymptotic scaling relation in RRBC. Recently, Grooms & Whitehead (2015) derived from the asymptotically reduced equations for $Ra\,Ek^{8/5} = O(1)$ in the limit of rapid rotation $Ek \to 0$ and strong thermal forcing $Ra \to \infty$, that there exists an upper bound on the heat transport in RRBC: $Nu \leq 20.56\,Ra^3 Ek^4$ for an infinite Prandtl number $Pr \to \infty$. A similar scaling relation was derived by King *et al.* (2012) via the marginal thermal boundary layer instability criterion, which can be viewed as an asymptotic state where the destabilising effect of buoyancy and stabilising effect of rotation are balanced at the edge of a thermal boundary layer. As demonstrated here, in the steep heat transfer regime, the kinetic energy dissipation rate ϵ_u is viscous-dependent when the flow is not fully turbulent.

Hence it is noteworthy that the present scaling argument provides a unified framework to derive both the geostrophic turbulence and steep heat transport scaling
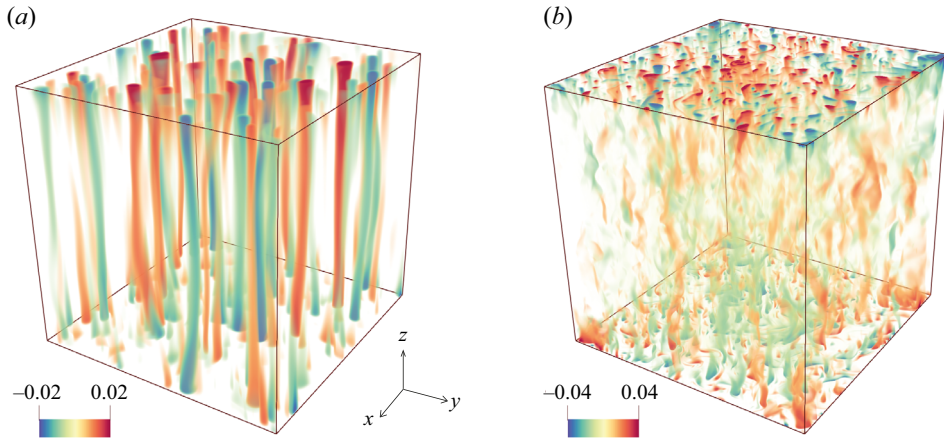
Figure 4. The thermal fluctuations $(\theta - \langle\theta\rangle_A)/\Delta$ illustrate (*a*) the Taylor columns at $Ra = 2.5 \times 10^{12}$, and (*b*) geostrophic turbulence at $Ra = 10^{13}$, in these two regimes for $Ek = 5 \times 10^{-9}$. Here, $\langle\cdot\rangle_A$ denotes the average in time and over any horizontal cross-section A. For clarity, the domains are stretched horizontally by a factor 8 (see also the supplementary movies available at https://doi.org/10.1017/jfm.2024.249).

regimes of rapidly RRBC. Thus we propose that with decreasing $\widetilde{Ra}$, the regime of geostrophic turbulence, (3.11)–(3.14), should undergo transition to another scaling regime, (3.18)–(3.21), and in both regimes, (3.18) should hold. And indeed, our DNS data fully support this. For smaller $\widetilde{Ra}$, $Nu - 1$ follows the relation (3.19), while for larger $\widetilde{Ra}$, it scales according to (3.12); see figure 2(*b*). The theory says that $Re\, Ek^{1/3}$ should scale as $\propto \widetilde{Ra}$ in the geostrophic turbulence regime (3.13), and as $\propto \widetilde{Ra}^{5/2}$ in the other regime (3.20), and indeed, the data in figure 2(*c*) support these scaling relations. Moreover, as elucidated in Appendix B, all the derived scaling relations for ϵ_u and $\tilde{\epsilon}_\theta$ also hold in both regimes. The typical flow structures in these two scaling regimes are shown in figure 4; they are Taylor columns and geostrophic turbulence, respectively. Obviously, the flows are dominated by the vertically aligned structures: columns and plumes. In contrast to non-rotating Rayleigh–Bénard convection, where a large-scale circulation spans the bottom and top walls in the flow field, the flow displays convective motions that have much smaller length scales compared to the domain size.

To quantify the quality of the agreement between the derived steep heat transport scaling relations and the DNS data, we also fit the exponents of the heat transport scaling $Nu - 1 \propto Ra^\alpha\, Ek^4$, the velocity scaling $Re \propto Ra^\beta\, Ek^3$, and the convective length scale scaling $\ell/L \propto Ra^\gamma\, Ek$, based on different Ra ranges of data points for $Ek = 5 \times 10^{-9}$. The results are listed in table 2. With 95 % confidence, the heat transport scaling exponent α ranges from 3.00 to 3.33, the momentum transport scaling exponent β ranges from 2.17 to 2.29, and the convective length scale scaling exponent γ ranges from 0.35 to 0.45, with variant fitting data points. As compared to the geostrophic turbulence regime, the value of the exponent α here is more sensitive to the fitting Ra range, but it gradually decreases to the predicted value when fitting with more data points. The values of the exponents β and γ do not differ much for different numbers of the fitting data points; they stay close to the predicted values.

It should be noted that near the onset of steady convection, the linear instability analysis gives the onset convective length scale $\ell/L \sim 4.8154\, Ek^{1/3} = L_c$ for $Pr \geq 0.68$ (Chandrasekhar 1953). As demonstrated in figure 5, the convective length scales calculated for the vertical velocity and temperature fluctuations at smaller values of

Theory	—	$\alpha = 3.0$	$\beta = 2.5$	$\gamma = 0.5$
Points	*Ra* range	α range	β range	γ range
4	1.5×10^{12}–2.1×10^{12}	3.33 ± 0.24	2.29 ± 0.19	0.35 ± 0.26
5	1.5×10^{12}–2.3×10^{12}	3.27 ± 0.17	2.28 ± 0.09	0.40 ± 0.18
6	1.5×10^{12}–2.5×10^{12}	3.21 ± 0.16	2.26 ± 0.07	0.45 ± 0.14
7	1.5×10^{12}–3.0×10^{12}	3.00 ± 0.28	2.17 ± 0.13	0.45 ± 0.09

Table 2. The theoretical and least squares fit exponents of $Nu - 1 \propto Ra^\alpha Ek^4$, $Re \propto Ra^\beta Ek^3$ and $\ell/L \propto Ra^\gamma Ek$ of the steep heat transport regime. The least squares fit is conducted at the smallest $Ek = 5 \times 10^{-9}$, with different data points, with 95 % confidence. The last data point is chosen at $Ra = 3.0 \times 10^{12}$, where the steep heat transport regime undergoes transition to the other regime.
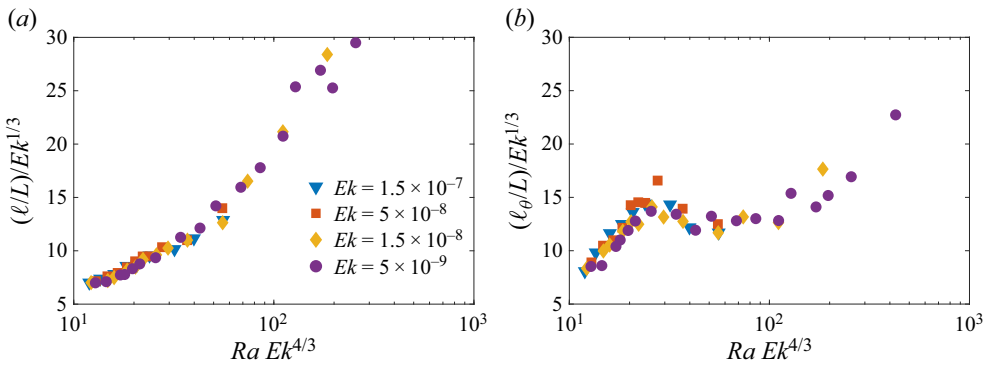

Figure 5. Dimensionless (*a*) convective length scale ℓ/L and (*b*) convective length scale ℓ_θ/L compensated with the onset length scale of $Ek^{1/3}$ as a function of $Ra\,Ek^{4/3}$.

the supercriticality parameter do show a trend towards the onset length scale $\sim Ek^{1/3}$. However, the compensated value converges to about 7 at the lowest studied value of the supercriticality parameter, which is slightly larger than the predicted value 4.8 for the onset wavelength. However, as demonstrated in Appendix C, the convective length scale ℓ/L used in figure 2(*a*) is very close to the onset length scale for the range of $Ra\,Ek^{4/3}/8.7 \leq 2$. In addition, as demonstrated in table 2, the scaling of the convective length scale gradually deviates from $Ra^{1/2}$ and changes into $Ra^{0.35}$ for the lower *Ra* range. This result is quite close to $Ra^{0.38}$ as reported by Madonia *et al.* (2021) (close to onset regime), who calculated the length scale based on the autocorrelation function of the vertical velocity. To this end, the convective length scale study conducted here clearly demonstrates that different definitions of the length scale can significantly affect the scaling results.

4. Conclusions

To sum up, based on our DNS of RRBC for extreme *Ra* and *Ek*, we have verified for the first time the existence and all the heat and momentum transport as well as the convective length scale (3.11)–(3.14) for the geostrophic turbulence regime. Furthermore, we have shown that this regime is connected to another rotation-dominated regime, (3.18)–(3.21), which can be achieved from geostrophic turbulence regime by decreasing the thermal driving (*Ra*), while keeping constant rotation (*Ek*). The principle difference between the

984 A45-10

two regimes is the different scaling of the kinetic energy dissipation rate: it is turbulent in one case and laminar in the other. Based on this conceptual framework, we proposed a scaling theory that unifies the two geostrophic regimes in RRBC. This theory can also be applied to derive scaling regimes in e.g. magnetoconvection while considering the Ohmic dissipation caused by the magnetic field.

Author ORCIDs.

Jiaxing Song https://orcid.org/0000-0002-9341-0345;

Olga Shishkina https://orcid.org/0000-0002-6773-6464;

Xiaojue Zhu https://orcid.org/0000-0002-7878-0655.

Appendix A. Numerical parameters and grid resolutions

Three-dimensional DNS are performed for a broad parameter range with the Rayleigh number in $1.5 \times 10^{10} \leq Ra \leq 3 \times 10^{13}$, Ekman number within $5 \times 10^{-9} \leq Ek \leq 1.5 \times 10^{-7}$, and Prandtl number $Pr = 1$. The DNS are conducted in domains with no-slip top and bottom as well as periodic lateral BCs, in order to avoid the effect of the wall modes (Rossby 1969; Favier & Knobloch 2020) or boundary zonal flows (Zhang *et al.* 2020; Wedi *et al.* 2022). The full characterization of the DNS parameters is presented in table 3.

No.	Ra	Re	Nu	Error	$N_z \times N_x \times N_y$
		$Ek = 1.5 \times 10^{-7}, \Gamma = 0.5$			
1	1.5×10^{10}	305.84	2.60	0.69 %	$512 \times 1024 \times 1024$
2	1.7×10^{10}	412.91	3.64	0.92 %	$512 \times 1024 \times 1024$
3	2.0×10^{10}	694.28	5.76	0.43 %	$576 \times 1152 \times 1152$
4	2.3×10^{10}	972.31	8.85	0.61 %	$576 \times 1152 \times 1152$
5	2.6×10^{10}	1263.31	12.14	0.65 %	$576 \times 1152 \times 1152$
6	3.0×10^{10}	1574.80	15.58	0.62 %	$576 \times 1152 \times 1152$
7	4.0×10^{10}	2185.96	21.51	0.74 %	$576 \times 1152 \times 1152$
8	5.0×10^{10}	2613.29	25.35	0.68 %	$576 \times 1152 \times 1152$
9	7.0×10^{10}	3523.38	34.38	0.68 %	$576 \times 1152 \times 1152$
		$Ek = 5.0 \times 10^{-8}, \Gamma = 0.25$			
10	7.0×10^{10}	557.91	2.85	0.77 %	$640 \times 480 \times 480$
11	8.0×10^{10}	766.67	4.05	0.20 %	$640 \times 480 \times 480$
12	9.0×10^{10}	1023.97	5.72	0.49 %	$640 \times 480 \times 480$
13	1.0×10^{11}	1312.23	7.75	0.75 %	$640 \times 480 \times 480$
14	1.1×10^{11}	1581.56	9.67	0.59 %	$768 \times 576 \times 576$
15	1.2×10^{11}	1837.88	11.57	0.48 %	$768 \times 576 \times 576$

Table 3. For caption see next page.

No.	Ra	Re	Nu	Error	$N_z \times N_x \times N_y$
16	1.3×10^{11}	2154.65	13.81	0.88 %	$769 \times 576 \times 576$
17	1.5×10^{11}	2611.26	17.03	0.48 %	$768 \times 576 \times 576$
18	2.0×10^{11}	3467.87	22.43	0.49 %	$768 \times 768 \times 768$
19	3.0×10^{11}	5024.47	32.66	0.69 %	$768 \times 768 \times 768$
		$Ek = 1.5 \times 10^{-8}$, $\Gamma = 0.25$			
20	3.3×10^{11}	674.93	2.29	0.09 %	$768 \times 768 \times 768$
21	4.0×10^{11}	1052.84	3.55	0.53 %	$768 \times 768 \times 768$
22	4.3×10^{11}	1234.60	4.25	0.80 %	$768 \times 768 \times 768$
23	5.0×10^{11}	1758.75	6.38	0.61 %	$768 \times 768 \times 768$
24	5.5×10^{11}	2141.51	8.14	0.37 %	$768 \times 768 \times 768$
25	6.0×10^{11}	2584.87	10.09	0.86 %	$768 \times 768 \times 768$
26	7.0×10^{11}	3338.80	13.49	0.33 %	$768 \times 768 \times 768$
27	8.0×10^{11}	4019.77	16.52	0.97 %	$864 \times 864 \times 864$
28	1.0×10^{12}	5044.37	20.75	0.70 %	$960 \times 960 \times 960$
29	1.5×10^{12}	7417.18	31.03	0.50 %	$960 \times 960 \times 960$
30	2.0×10^{12}	10 059.86	44.16	0.30 %	$960 \times 960 \times 960$
31	3.0×10^{12}	15 946.86	76.32	0.40 %	$960 \times 960 \times 960$
32	5.0×10^{12}	27 142.35	147.80	0.36 %	$1280 \times 1280 \times 1280$
		$Ek = 5.0 \times 10^{-9}$, $\Gamma = 0.125$			
33	1.5×10^{12}	1007.03	2.37	0.43 %	$960 \times 480 \times 480$
34	1.7×10^{12}	1339.29	3.10	0.43 %	$960 \times 480 \times 480$
35	2.0×10^{12}	1969.28	4.64	0.43 %	$960 \times 480 \times 480$
36	2.1×10^{12}	2153.16	5.17	0.61 %	$960 \times 480 \times 480$
37	2.3×10^{12}	2674.97	6.54	0.45 %	$960 \times 480 \times 480$
38	2.5×10^{12}	3179.17	8.02	0.68 %	$960 \times 480 \times 480$
39	3.0×10^{12}	4444.58	11.73	0.61 %	$960 \times 480 \times 480$
40	4.0×10^{12}	6538.48	17.88	0.90 %	$960 \times 480 \times 480$
41	5.0×10^{12}	8123.64	22.30	0.58 %	$960 \times 480 \times 480$
42	6.0×10^{12}	9730.18	27.13	0.15 %	$960 \times 480 \times 480$
43	8.0×10^{12}	13 097.65	38.07	0.66 %	$960 \times 480 \times 480$
44	1.0×10^{13}	16 720.54	51.44	0.50 %	$1024 \times 512 \times 512$
45	1.3×10^{13}	22 567.14	74.42	0.79 %	$1024 \times 512 \times 512$
46	1.5×10^{13}	27 404.78	91.45	0.68 %	$1536 \times 768 \times 768$
47	2.0×10^{13}	38 549.57	144.19	0.23 %	$2048 \times 1024 \times 1024$
48	2.3×10^{13}	44 739.22	175.82	0.50 %	$2048 \times 1024 \times 1024$
49	3.0×10^{13}	59 640.19	245.06	0.42 %	$2048 \times 1024 \times 1024$

Table 3. Summary of the quantities in the present DNS of RRBC. All simulations are performed at $Pr = 1$. Here, Ra is the Rayleigh number, Re is the Reynolds number, Ek is the Ekman number, and $\Gamma = D/L$ is the aspect ratio, where D is the horizontal period and L is the domain height. The averaged Nusselt number Nu is calculated from the Nu values evaluated in five different ways: at the bottom and top plates, by volume-averaging, from the kinetic energy, and from thermal dissipation rates. The 'Error' denotes the maximum relative error between each two of these values. The last column represents the grid mesh sizes used in the vertical (N_z) and two horizontal (N_x, N_y) directions.

Appendix B. Dissipation rates scaling regimes

As the dissipation rates and their scaling relations in the main text are fundamental blocks to our theoretical derivations, we show both the kinetic energy and thermal dissipation rates as functions of $Ra \, Ek^{4/3}$ in figure 6. Specifically, the kinetic energy dissipation rate should scale as (3.14) in the geostrophic turbulence regime, and (3.21) in the steep heat
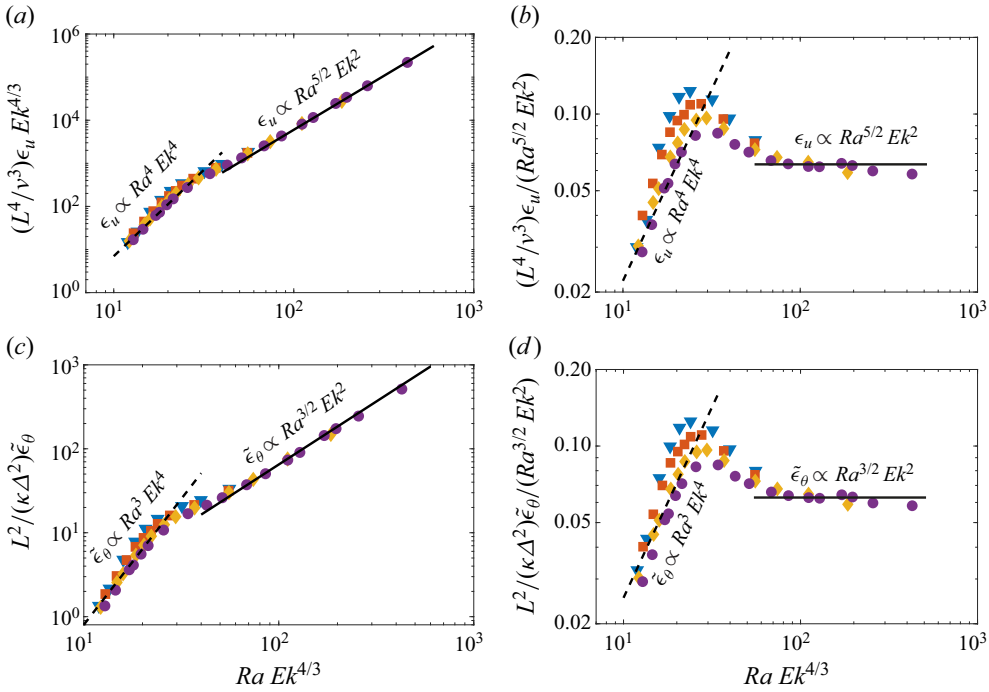
984 A45-12

Figure 6. The dependence on $\widetilde{Ra}$ of the time- and volume-averaged (a,b) kinetic dissipation rate ϵ_u, and (c,d) convective thermal dissipation rate $\tilde{\epsilon}_\theta \equiv \epsilon_\theta - \kappa \Delta^2/L^2$. ($a$) For larger $\widetilde{Ra}$, ϵ_u scales as expected for the geostrophic turbulence regime: $\epsilon_u \propto Ra^{5/2} Ek^2$ (solid line), while for smaller $\widetilde{Ra}$, it scales as $\epsilon_u \propto Ra^4 Ek^4$ (dashed line). (b) Here, ϵ_u is normalized by $Ra^{5/2} Ek^2$. (c) For larger $\widetilde{Ra}$, $\tilde{\epsilon}_\theta$ scales as expected for the geostrophic turbulence regime, $\tilde{\epsilon}_\theta \propto Ra^{3/2} Ek^2$ (solid line), while for smaller $\widetilde{Ra}$, it scales as $\tilde{\epsilon}_\theta \propto Ra^3 Ek^4$ (dashed line). (d) Here, $\tilde{\epsilon}_\theta$ is normalized by $Ra^{3/2}Ek^2$. Symbols have the same meanings as in figure 1.

transport regime, respectively. As demonstrated in figures 6(a,b), these two derived scaling relations for ϵ_u are verified in both regimes. On the other hand, for the convective thermal dissipation rate, it is supposed to follow the same equations as for $Nu - 1$, i.e. (3.12) in the geostrophic turbulence regime, and (3.19) in the steep heat transport regime, respectively. To this end, as shown in figures 6(c,d), these two scaling relations for $\tilde{\epsilon}_\theta$ are also verified in both regimes.

Appendix C. Approach to the onset length scale

In order to further demonstrate how the current results approach the actual onset wavelength, following the procedure of Nieves, Rubio & Julien (2014) and Madonia *et al.* (2021), we calculate the spatial autocorrelation function of the vertical velocity at the middle height ($z = 0.5$) as follows

$$\text{Corr}(\Delta x) = \frac{\langle u_z'(x, t)\, u_z'(x + \Delta x, t)\rangle}{\langle u_z'^2(x, t)\rangle}. \tag{C1}$$

Here, u_z' is the fluctuation part of the vertical velocity u_z, and Δx is the separate spatial distance in the horizontal directions (x or y). When we calculate the autocorrelation function in the x (y) direction, $\langle \cdot \rangle$ denotes the average in the y (x) direction (i.e. in another horizontal direction). Actually, the autocorrelation functions in the two horizontal
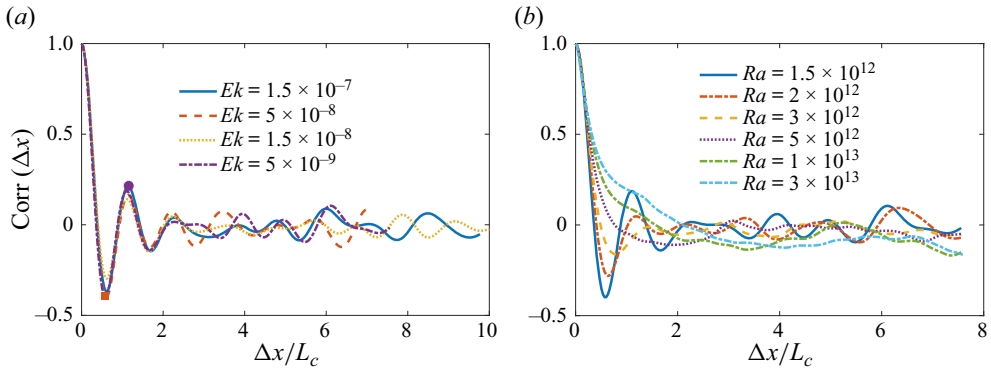
984 A45-13

Figure 7. (*a*) Spatial (*x* direction) autocorrelation function of vertical velocity for the lowest *Ra* for different *Ek*. (*b*) Spatial (*x* direction) autocorrelation function of vertical velocity for different *Ra* at $Ek = 5 \times 10^{-9}$.

directions show very similar results. As demonstrated in figure 7(*a*), for the lowest *Ra* for each *Ek*, the autocorrelation functions show distinguished extrema for separate spatial distances, especially for $\Delta x/L_c \leq 2$. Specifically, according to Nieves *et al.* (2014), the first maximum in the autocorrelation signals occurs at the critical length scale ($\Delta x/L_c \approx 1$), which is also observed in the current dataset. Consistent with Nieves *et al.* (2014), the autocorrelation function calculated by temperature fluctuation displays very similar results as for the vertical velocity (not shown here). On the other hand, at constant *Ek*, as depicted in figure 7(*b*) with increasing *Ra*, the autocorrelation function gradually smoothes out and the peaks are not distinguishable. This impedes attempts to use this method to quantify the convective length scale for high $Ra\,Ek^{4/3}$ at plumes and geostrophic turbulence regimes. Nevertheless, based on the autocorrelation function, the locations at the first maximum/minimum or the zero values have been used to quantify the typical convective length scale. In the study of Madonia *et al.* (2021), the length scales calculated by different quantities with different locations displayed very different scaling relations. For the plumes and geostrophic turbulence regimes ($Ra/Ra_c > 5$), the length scale defined by the spatial autocorrelations of the vertical velocity (the first zero location) shows a scaling of $Ra^{0.38}$, while the length scale calculated by the integral of the autocorrelation function seems to have a different scaling behaviour. For the lower supercriticality ($Ra/Ra_c \leq 5$) at the columnar regime, both length scales seem to be constant.

In figure 8, we show the convective length scale evaluated by the first minimum/maximum value locations (marked as an orange square/purple circle in figure 7*a*) in the autocorrelation functions of the vertical velocity. But we show only the results for $Ra\,Ek^{4/3}/8.7 \leq 2$ where these peaks are distinguished. For ℓ_{min}/L in figure 8(*a*), the compensated value is approximately 3 and remains constant in the range $Ra\,Ek^{4/3}/8.7 \leq 2$. This implies that the length scale ℓ_{min}/L follows the onset length scale very well in this range. If we choose the first maximum value location to evaluate the length scale, then the compensated value of ℓ_{max}/L in figure 8(*b*) increases slightly from 5 to 6.5 for the range $Ra\,Ek^{4/3}/8.7 \leq 2$. This value is very close to the compensated value 7 of length scale ℓ/L calculated by the spectra method (see figure 5*a*), where the ensemble integral operation is used. This demonstrates clearly that different definitions of the length scale can significantly affect the scaling results. Hence the convective length scale ℓ/L used in figure 2(*a*) is very close to the onset length scale for the range $Ra\,Ek^{4/3}/8.7 \leq 2$.
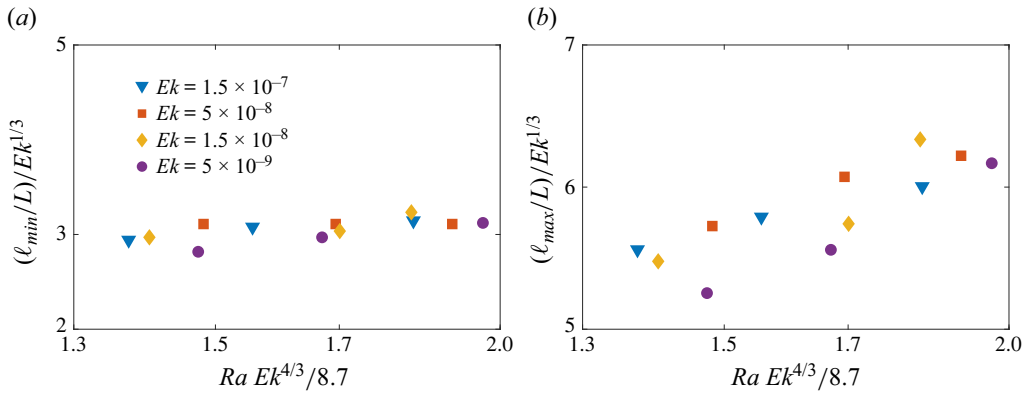
984 A45-14

Figure 8. Dimensionless convective length scale (*a*) ℓ_{min}/L and (*b*) ℓ_{max}/L compensated with $Ek^{1/3}$ as a function of $Ra\,Ek^{4/3}/8.7$ for $Ra\,Ek^{4/3}/8.7 \leq 2$. Here, ℓ_{min}/L is evaluated by the average of the first minimum value locations (marked as an orange square in figure 7*a*) in the *x* and *y* autocorrelation functions of vertical velocity; ℓ_{max}/L is evaluated by the average of the first maximum value locations (marked as a purple circle in figure 7*a*) in the *x* and *y* autocorrelation functions of vertical velocity.

REFERENCES

AGUIRRE GUZMÁN, A.J., MADONIA, M., CHENG, J.S., OSTILLA-MÓNICO, R., CLERCX, H.J.H. & KUNNEN, R.P.J. 2021 Force balance in rapidly rotating Rayleigh–Bénard convection. *J. Fluid Mech.* **928**, A16.

AHLERS, G., GROSSMANN, S. & LOHSE, D. 2009 Heat transfer and large scale dynamics in turbulent Rayleigh–Bénard convection. *Rev. Mod. Phys.* **81**, 503.

AURNOU, J.M., CALKINS, M.A., CHENG, J.S., JULIEN, K., KING, E.M., NIEVES, D., SODERLUND, K.M. & STELLMACH, S. 2015 Rotating convective turbulence in Earth and planetary cores. *Phys. Earth Planet. Inter.* **246**, 52–71.

AURNOU, J.M., HORN, S. & JULIEN, K. 2020 Connections between nonrotating, slowly rotating, and rapidly rotating turbulent convection transport scalings. *Phys. Rev. Res.* **2**, 043115.

BADER, S.H. & ZHU, X. 2023 Scaling relations in quasi-static magnetoconvection with a strong vertical magnetic field. *J. Fluid Mech.* **974**, A4.

BOUBNOV, B.M. & GOLITSYN, G.S. 1990 Temperature and velocity field regimes of convective motions in a rotating plane fluid layer. *J. Fluid Mech.* **219**, 215–239.

BOUILLAUT, V., MIQUEL, B., JULIEN, K., AUMAÎTRE, S. & GALLET, B. 2021 Experimental observation of the geostrophic turbulence regime of rapidly rotating convection. *Proc. Natl Acad. Sci. USA* **118**, 44.

BUSSE, F.H. & CARRIGAN, C.R. 1976 Laboratory simulation of thermal convection in rotating planets and stars. *Science* **191**, 81–83.

CHANDRASEKHAR, S. 1953 The instability of a layer of fluid heated below and subject to Coriolis forces. *Proc. R. Soc. Lond.* A **217**, 306–327.

CHENG, J.S. & AURNOU, J.M. 2016 Tests of diffusion-free scaling behaviors in numerical dynamo datasets. *Earth Planet Sci. Lett.* **436**, 121–129.

CHENG, J.S., AURNOU, J.M., JULIEN, K. & KUNNEN, R.P.J. 2018 A heuristic framework for next-generation models of geostrophic convective turbulence. *Geophys. Astrophys. Fluid Dyn.* **112**, 277–300.

CHENG, J.S., STELLMACH, S., RIBEIRO, A., GRANNAN, A., KING, E.M. & AURNOU, J.M. 2015 Laboratory-numerical models of rapidly rotating convection in planetary cores. *Geophys. J. Intl* **201**, 1–17.

ECKE, R., ZHONG, F. & KNOBLOCH, E. 1992 Hopf bifurcation with broken reflection symmetry in rotating Rayleigh–Bénard convection. *Europhys. Lett.* **19** (3), 177–182.

ECKE, R.E. & SHISHKINA, O. 2023 Turbulent rotating Rayleigh–Bénard convection. *Annu. Rev. Fluid Mech.* **55**, 603–638.

ECKE, R.E., ZHANG, X. & SHISHKINA, O. 2022 Connecting wall modes and boundary zonal flows in rotating Rayleigh–Bénard convection. *Phys. Rev. Fluids* **7**, L011501.

FAVIER, B. & KNOBLOCH, E. 2020 Robust wall states in rapidly rotating Rayleigh–Bénard convection. *J. Fluid Mech.* **895**, R1.

GASTINE, T., WICHT, J. & AUBERT, J. 2016 Scaling regimes in spherical shell rotating convection. *J. Fluid Mech.* **808**, 690–732.

GILLET, N. & JONES, C.A. 2006 The quasi-geostrophic model for rapidly rotating spherical convection outside the tangent cylinder. *J. Fluid Mech.* **554**, 343–369.

GROOMS, I. & WHITEHEAD, J. 2015 Bounds on heat transport in rapidly rotating Rayleigh–Bénard convection. *Nonlinearity* **28**, 29–41.

GUERVILLY, C., CARDIN, P. & SCHAEFFER, N. 2019 Turbulent convective length scale in planetary cores. *Nature* **570**, 368–371.

GUERVILLY, C., HUGHES, D.W. & JONES, C.A. 2014 Large-scale vortices in rapidly rotating Rayleigh–Bénard convection. *J. Fluid Mech.* **758**, 407–435.

HERRMANN, J. & BUSSE, F.H. 1993 Asymptotic theory of wall-attached convection in a rotating fluid layer. *J. Fluid Mech.* **255**, 183–194.

JONES, C.A. 2011 Planetary magnetic fields and fluid dynamos. *Annu. Rev. Fluid Mech.* **43**, 583–614.

JULIEN, K., AURNOU, J.M., CALKINS, M.A., KNOBLOCH, E., MARTI, P., STELLMACH, S. & VASIL, G.M. 2016 A nonlinear model for rotationally constrained convection with Ekman pumping. *J. Fluid Mech.* **798**, 50–87.

JULIEN, K., KNOBLOCH, E., RUBIO, A.M. & VASIL, G.M. 2012*a* Heat transport in low-Rossby-number Rayleigh–Bénard convection. *Phys. Rev. Lett.* **109**, 254503.

JULIEN, K., RUBIO, A.M., GROOMS, I. & KNOBLOCH, E. 2012*b* Statistical and physical balances in low Rossby number Rayleigh–Bénard convection. *Geophys. Astrophys. Fluid Dyn.* **106**, 392–428.

KING, E.M., STELLMACH, S. & AURNOU, J.M. 2012 Heat transfer by rapidly rotating Rayleigh–Bénard convection. *J. Fluid Mech.* **691**, 568–582.

KUNNEN, R.P.J. 2021 The geostrophic regime of rapidly rotating turbulent convection. *J. Turbul.* **22**, 267–296.

LANDAU, L.D. & LIFSHITZ, E.M. 1987 *Fluid Mechanics*, 2nd edn, Course of Theoretical Physics, vol. 6. Butterworth Heinemann.

LU, H.-R., DING, G.-Y., SHI, J.-Q., XIA, K.-Q. & ZHONG, J.-Q. 2021 Heat-transport scaling and transition in geostrophic rotating convection with varying aspect ratio. *Phys. Rev. Fluids* **6**, L071501.

MADONIA, M., GUZMÁN, A.J.A., CLERCX, H.J.H. & KUNNEN, R.P.J. 2021 Velocimetry in rapidly rotating convection: spatial correlations, flow structures and length scales. *Europhys. Lett.* **135**, 54002.

MADONIA, M., GUZMÁN, A.J.A., CLERCX, H.J.H. & KUNNEN, R.P.J. 2023 Reynolds number scaling and energy spectra in geostrophic convection. *J. Fluid Mech.* **962**, A36.

MAFFEI, S., KROUSS, M.J., JULIEN, K. & CALKINS, M.A. 2021 On the inverse cascade and flow speed scaling behaviour in rapidly rotating Rayleigh–Bénard convection. *J. Fluid Mech.* **913**, A18.

MALKUS, M.V.R. 1954 The heat transport and spectrum of thermal turbulence. *Proc. R. Soc. Lond.* A **225**, 196–212.

NIEVES, D., RUBIO, A.M. & JULIEN, K. 2014 Statistical classification of flow morphology in rapidly rotating Rayleigh–Bénard convection. *Phys. Fluids* **26**, 086602.

PLUMLEY, M. & JULIEN, K. 2019 Scaling laws in Rayleigh–Bénard convection. *Earth Space Sci.* **34**, 1580–1592.

PLUMLEY, M., JULIEN, K., MARTI, P. & STELLMACH, S. 2017 Sensitivity of rapidly rotating Rayleigh–Bénard convection to Ekman pumping. *Phys. Rev. Fluids* **2**, 094801.

VAN DER POEL, E.P., OSTILLA-MÓNICO, R., DONNERS, J. & VERZICCO, R. 2015 A pencil distributed finite difference code for strongly turbulent wall-bounded flows. *Comput. Fluids* **116**, 10–16.

PRIESTLEY, C.H.B. 1959 *Turbulent Transfer in the Lower Atmosphere*. University of Chicago Press.

ROSSBY, T.H. 1969 A study of Bénard convection with and without rotation. *J. Fluid Mech.* **36**, 309–335.

SCHMITZ, S. & TILGNER, A. 2009 Heat transport in rotating convection without Ekman layers. *Phys. Rev.* E **80**, 0015305(R).

SHISHKINA, O. 2020 Tenacious wall states in thermal convection in rapidly rotating containers. *J. Fluid Mech.* **898**, F1.

SHISHKINA, O., STEVENS, R.J.A.M., GROSSMANN, S. & LOHSE, D. 2010 Boundary layer structure in turbulent thermal convection and its consequences for the required numerical resolution. *New J. Phys.* **12**, 075022.

SPRAGUE, M., JULIEN, K., KNOBLOCH, E. & WERNE, J. 2006 Numerical simulation of an asymptotically reduced system for rotationally constrained convection. *J. Fluid Mech.* **551**, 141–174.

STELLMACH, S., LISCHPER, M., JULIEN, K., VASIL, G., CHENG, J.S., RIBEIRO, A., KING, E.M. & AURNOU, J.M. 2014 Approaching the asymptotic regime of rapidly rotating convection: boundary layers versus interior dynamics. *Phys. Rev. Lett.* **113**, 254501.

STEVENS, R.J.A.M., CLERCX, H.J.H. & LOHSE, D. 2013 Heat transport and flow structure in rotating Rayleigh–Bénard convection. *Eur. J. Mech.* B*/Fluids* **40**, 41–49.

STEVENSON, D.J. 1979 Turbulent thermal convection in the presence of rotation and a magnetic field – a heuristic theory. *Geophys. Astrophys. Fluid Dyn.* **12**, 139–169.

VERZICCO, R. & ORLANDI, P. 1996 A finite-difference scheme for three-dimensional incompressible flows in cylindrical coordinates. *J. Comput. Phys.* **123**, 402–414.

WANG, G., SANTELLI, L., LOHSE, D., VERZICCO, R. & STEVENS, R.J.A.M. 2021 Diffusion-free scaling in rotating spherical Rayleigh–Bénard convection. *Geophys. Res. Lett.* **48**, e2021GL095017.

WEDI, M., MOTURI, V.M., FUNFSCHILLING, D. & WEISS, S. 2022 Experimental evidence for the boundary zonal flow in rotating Rayleigh–Bénard convection. *J. Fluid Mech.* **939**, A14.

WICHT, J. & SANCHEZ, S. 2019 Advances in geodynamo modelling. *Geophys. Astrophys. Fluid Dyn.* **113** (1–2), 2–50.

DE WIT, X.M., AGUIRRE GUZMÁN, A.J., MADONIA, M., CHENG, J.S., CLERCX, H.J.H. & KUNNEN, R.P.J. 2020 Turbulent rotating convection confined in a slender cylinder: the sidewall circulation. *Phys. Rev. Fluids* **5**, 023502.

DE WIT, X.M., AGUIRRE GUZMÁN, A.J., MADONIA, M., CHENG, J.S., CLERCX, H.J.H. & KUNNEN, R.P.J. 2022 Discontinuous transitions towards vortex condensates in buoyancy-driven rotating turbulence. *J. Fluid Mech.* **963**, A43.

DE WIT, X.M., BOOT, W.J.M., MADONIA, M., GUZMÁN, A.J.A. & KUNNEN, R.P.J. 2023 Robust wall modes and their interplay with bulk turbulence in confined rotating Rayleigh–Bénard convection. *Phys. Rev. Fluids*. **8**, 073501.

ZHANG, X., ECKE, R.E. & SHISHKINA, O. 2021 Boundary zonal flows in rapidly rotating turbulent thermal convection. *J. Fluid Mech.* **915**, A62.

ZHANG, X., VAN GILS, D.P.M., HORN, S., WEDI, M., ZWIRNER, L., AHLERS, G., ECKE, R.E., WEISS, S., BODENSCHATZ, E. & SHISHKINA, O. 2020 Boundary zonal flows in rotating turbulent Rayleigh–Bénard convection. *Phys. Rev. Lett.* **124**, 084505.

ZHU, X., *et al.* 2018 AFiD-GPU: a versatile Navier–Stokes solver for wall-bounded turbulent flows on GPU clusters. *Comput. Phys. Commun.* **229**, 199–210.